Available online at www.sciencedirect.com

SCIENCE DIRECT®

International Journal of Heat and Mass Transfer 48 (2005) 191–209

International Journal of HEAT and MASS TRANSFER

www.elsevier.com/locate/ijhmt

Double-diffusive natural convection in an asymmetric trapezoidal enclosure: unsteady behavior in the laminar and the turbulent-flow regime

E. Papanicolaou [*], V. Belessiotis

"Demokritos" National Center for Scientific Research, Solar and other Energy Systems Laboratory,
Aghia Paraskevi, Attiki 15310, Greece

Received 6 January 2004
Available online 18 October 2004

Abstract

In the present work the natural convective heat and mass transfer in an asymmetric, trapezoidal enclosure is studied numerically. Such a configuration is encountered in greenhouse-type solar stills, where natural convection in the enclosed humid air due to vertical temperature and concentration gradients between the saline water and the transparent cover, plays a decisive role. In this double-diffusion problem, the relative magnitude of the thermal and the concentration (or solutal) Rayleigh numbers, expressed by their ratio N is a key parameter. The two-dimensional flow equations, expressed here in a stream function-vorticity ($\Psi - \Omega$) formulation, along with the energy and concentration equations are solved. Due to the large values of the Rayleigh numbers encountered under realistic conditions ($10^7 \leqslant Ra \leqslant 10^{10}$), mostly turbulent flow conditions prevail. A two-equation, low-Reynolds number turbulence model has thus been selected and a curvilinear coordinate system is employed, allowing for better matching of the computational grid to the enclosure geometry. The numerical solutions yield a multi-cellular flow field, with the number of cells depending on the Rayleigh number for a fixed Lewis number and geometry. For a positive value of N ($N = 1$) the solution is qualitatively similar to the case with only thermal buoyancy present ($N = 0$). However, for negative values ($N = -1$), more complex unsteady phenomena arise, having a different nature in the laminar and the turbulent flow regime, which are both investigated. Correlations for the mean convective heat and mass transfer coefficients are obtained for a wide range of Rayleigh numbers, and comparisons are made for the different values of N, showing lower values and different rate of increase with Ra for $N = -1$.

1. Introduction

Natural convection in enclosed spaces of various forms occupies a large portion of the heat transfer literature, reflecting the large number of investigations on the subject that have been undertaken over the years. In the vast majority of cases, rectangular or cylindrical geometries have been considered. A smaller number of studies have considered the trapezoidal geometry, which is encountered in several practical applications, such as attic spaces in buildings [1], greenhouses [2] or sun drying of crops [3]. Fundamental studies on natural convection in trapezoidal enclosures of various forms

---

[*] Corresponding author. Tel.: +30 1 650 3817; fax: +30 1 654 4592.
E-mail address: elpapa@ipta.demokritos.gr (E. Papanicolaou).

0017-9310/$ - see front matter © 2004 Elsevier Ltd. All rights reserved.
doi:10.1016/j.ijheatmasstransfer.2004.07.040

Nomenclature

A	dimensionless average height (or aspect ratio) of the enclosure $A = H_m/L$
C	vapor concentration (kg vapor/kg humid air)
D	mass diffusivity for vapor (m^2/s)
g	magnitude of the gravitational acceleration (m/s^2)
H	maximum vertical height of the enclosure (m)
H_1	height of the vertical side walls of the enclosure (m)
H_m	average height of the enclosure $H_m = 0.5 \times (H + H_1)$ (m)
$\mathbf{J}$	Jacobian of the coordinate transformation matrix $\mathbf{J} = \det(\partial x_i/\partial \xi_j)$
k	turbulent kinetic energy non-dimensionalized by $(\alpha/L)^2$
L	length of base of the enclosure (m)
Le	lewis number $Le = \alpha/D = Sc/Pr$
N	ratio of buoyancy forces $N = \beta^*\Delta C/\beta\Delta T = Ra_C/Ra$
Nu	Nusselt number averaged over a surface $Nu = \int_0^1 Nu_s \, ds$
Nu_s	local Nusselt number varying along a surface $Nu_s = (\partial\theta/\partial n)_w$
Pr	Prandtl number of air $Pr = \nu/\alpha$
Ra_C	concentration Rayleigh number based on the enclosure base $Ra = g\beta^*\Delta CL^3/\nu\alpha$
Ra	thermal Rayleigh number based on the enclosure base $Ra = g\beta\Delta TL^3/\nu\alpha$
Ra_m	thermal Rayleigh number based on the average height H_m of the enclosure $Ra_m = g\beta\Delta TH_m^3/\nu\alpha = A^3Ra$
Sc	Schmidt number $Sc = \nu/D$
Sh	Sherwood number averaged over a surface $Sh = \int_0^1 sh_s \, ds$
Sh_s	local Sherwood number varying along a surface $Sh_s = (\partial C/\partial n)_w$
t	physical time (s)
T	local temperature (K)
x, y	vertical and horizontal Cartesian coordinate distance, respectively (m)
X, Y (or X_i)	dimensionless vertical and horizontal Cartesian coordinate distance, respectively, $X = x/L$, $Y = y/L$
u, v	vertical and horizontal Cartesian velocity components, respectively (m/s)
U, V	dimensionless Cartesian velocity components $(U, V) = (u/(\alpha/L), v/(\alpha/L))$

Greek symbols

α	thermal diffusivity of air (m^2/s)
α_t	Eddy diffusivity for heat
β	volumetric Coefficient of thermal expansion $\beta \equiv -(1/\rho)(\partial_\rho/\partial T)_p(K^{-1})$
β^*	volumetric coefficient of expansion with concentration $\beta^* \equiv -(1/\rho)(\partial_\rho/\partial C)_p$ (kg^{-1})
ΔC	vertical concentration difference $\Delta C = C_b - C_t$
ΔT	vertical temperature difference $\Delta T = T_b - T_t$
ϵ	rate of dissipation of the turbulent kinetic energy, non-dimensionalized by $(\alpha/L)^3/L$
θ	dimensionless temperature $\theta = (T - T_t)/\Delta T$
ξ, η (or ξ_j)	coordinates in the curvilinear (transformed system)
ν	kinematic viscosity of air (m^2/s)
ν_t	turbulent viscosity (m^2/s)
σ_ϵ, σ_k	Prandtl number for the turbulent kinetic energy and its rate of dissipation respectively
σ_C	turbulent Schmidt number $\sigma_C = D/\alpha_t$
σ_T	turbulent Prandtl number $\sigma_T = \nu_t/\alpha_t$
τ	dimensionless time $\tau = t/(L^2/\alpha)$
Ψ	dimensionless stream function $U = -\partial\Psi/\partial Y$, $V = \partial\Psi/\partial X$
Ω	dimensionless vorticity $\Omega = \partial V/\partial X - \partial U/\partial Y$

Subscripts

i	initial value
b	value of a variable at the bottom boundary
t	value of a variable at the top boundary

(including triangular ones as a special case) have been presented by Poulikakos and Bejan [4], Lam et al. [5], Lee [6], Perić [7], Salmun [8] and Kuyper and Hoogendoorn [9]. A particularly interesting area where such a geometry is involved is the distillation of saline water in greenhouse-type solar stills [10,11], where the process is strongly influenced by the natural convective flow and transport. Few researchers have presented results on the associated flow and heat transfer problem, considering either symmetric [12,13] or single-slope still geometries [14]. In a recent study, Papanicolaou et al. [15] have presented numerical results for the flow and temperature fields in an asymmetric greenhouse-type solar still and demonstrated the effect of physical and geometric parameters, typical during a 24-h cycle of operation. In the space enclosed between the top inclined covers and the surface of saline water humid air circulates, therefore in addition to thermal effects there are also buoyant forces arising from the density differences due to gradients of the water vapor concentration. A more realistic numerical simulation effort, therefore, can be obtained if the air enclosed in the trapezoidal space is taken as a binary mixture, thus giving rise to a problem of double-diffusive (or thermosolutal) convection.

The fundamental problem of double-diffusive convection in enclosures has received attention mostly over the past decade. As far as rectangular enclosures are concerned, results have been presented, among others, by Wee et al. [16] and Béghein et al. [17]. The former study considered both vertical and horizontal cavities of aspect ratio 7 for the system air/water vapor, in an effort to simulate moisture transfer in building cavities. Both numerical and experimental results were obtained and correlations for the Nusselt and Sherwood numbers in terms of Grashof number were derived. Béghein et al. obtained steady-state numerical results for laminar flow in an air-filled square cavity for different Lewis and Rayleigh numbers and both opposing and assisting flows. In trapezoidal geometries, mostly numerical studies are available, such as those by Dong and Ebadian [18] and Boussaid et al. [19,20] in the laminar-flow regime and by Van der Eyden et al. [21] in the turbulent flow regime. In Ref. [18] the configuration was an enclosure with 75° inclined side walls and horizontal top and bottom and steady numerical solutions were obtained with lateral thermal and solutal gradients for $Pr = 7$ and $Le = 100$ (aqueous solution) and both opposing and assisting buoyancy forces. In Refs. [19,20], an enclosure with a single inclined surface at the top was considered, at various angles of inclination and Lewis numbers, and in which vertical temperature and concentration gradients were imposed. The binary fluid was air/water vapor and numerical results were obtained for assisting buoyancy forces, the majority of which was at $N = 1$. For thermal Rayleigh numbers (based on height) $Ra \geqslant 2 \times 10^5$ periodic oscillations were observed, which were damped at large times for up to $Ra = 3 \times 10^6$ but sustained beyond that value. The study by Van der Eyden et al. [21] considered a mixture of two gases in a trapezoidal enclosure with horizontal top and bottom and inclined side walls at 45°, a configuration encountered in underground coal gasification. They presented numerical results for the mixture argon/nitrogen with $Le = 1.16$ and for turbulent flow at thermal $Gr = 2.6 \times 10^8$ and $N = 2.5$, with gas injection from the bottom and the side walls and compared with experimental results. They also observed an oscillatory behavior at these conditions.

Particularly interesting phenomena occur when the two buoyancy forces, i.e., those due to thermal and solutal effects, are opposing each other and the buoyancy ratio N is negative. Such configurations, where the driving temperature are concentration gradients may be applied either in the horizontal or in the vertical direction, are prone to instabilities and bifurcation phenomena. In the case of rectangular enclosures and horizontally applied gradients, the studies by Ghorayeb and Mojtabi [22], Xin et al. [23], Bergeon et al. [24] and Ghorayeb et al. [25] have presented comprehensive results as far as the nature of the bifurcations and the respective critical values for their onset. The influence of the aspect ratio, Lewis number and angle of inclination have been investigated. However, oscillatory phenomena have been observed also for vertically imposed gradients in rectangular geometries by Mamou et al. [26] and, as already mentioned above, in trapezoidal geometries [20,21]. This is the case in the present configuration as well. The geometry and characteristic dimensions of the solar still which gave the motivation for this work are shown in Fig. 1a. Clearly, in the actual configuration the physical phenomena involved are quite complex and not all of them can be included in the present study. Here the focus is on the fundamental problem of the double-diffusive natural convection in such a geometry and in identifying the basic phenomena that develop due to the application of vertical temperature and concentration gradients and for buoyancy forces that are either assisting or opposing each other. The study

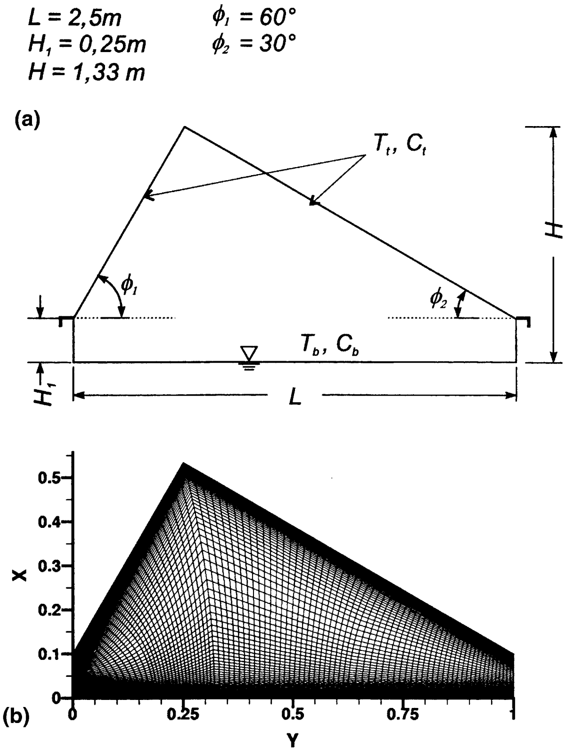

Fig. 1. (a) Geometry of the enclosure under consideration with characteristic dimensions and (b) grid in dimensionless coordinates.

focuses mostly on the turbulent-flow regime, which is the most common situation in the given practical application and since this was also the case in the previous work where only thermal buoyancy was present [15] and which the present work aims at extending. However, the unsteady phenomena that are present for $N < 0$, especially in view of Refs. [20,22–25], and which correspond to a specific mode of operation in a solar still as will be explained below, made an extension into lower Rayleigh numbers and laminar-flow computations indispensable for the sake of completeness of the study.

2. Mathematical model

2.1. Model equations

The mathematical model is based on the vorticity-stream function formulation for the solution of the flow field, coupled with the energy and concentration equations. In the turbulent- flow simulations the equations for the turbulence variables k and ϵ are also solved. The vorticity-stream function method, although so far not widely used for two-dimensional computations in curvilinear coordinates, is still quite an attractive option for natural convection problems, especially when the pressure field itself is not of particular interest. The model consists of the transformed Poisson-type stream function equation:

$$\frac{B_{11}}{\mathbf{J}^2}\frac{\partial^2\Psi}{\partial\xi^2}+\frac{B_{22}}{\mathbf{J}^2}\frac{\partial^2\Psi}{\partial\eta^2}+2\frac{B_{12}}{\mathbf{J}^2}\frac{\partial^2\Psi}{\partial\xi\partial\eta}+P\frac{\partial\Psi}{\partial\xi}+Q\frac{\partial\Psi}{\partial\eta}=-\Omega \tag{1}$$

along with the time-dependent transport equations for the variables: Ω, θ, C, K and ϵ. These are of the convection–diffusion type and can be written in the following common form:

$$\begin{aligned}\mathbf{J}\frac{\partial\phi}{\partial\tau}&+\frac{\partial}{\partial\xi}\left[U_1\phi-\Gamma_\phi\frac{B_{11}}{\mathbf{J}}\frac{\partial\phi}{\partial\xi}\right]+\frac{\partial}{\partial\eta}\left[U_2\phi-\Gamma_\phi\frac{B_{22}}{\mathbf{J}}\frac{\partial\phi}{\partial\eta}\right]\\&=\frac{\partial}{\partial\xi}\left(\Gamma_\phi\frac{B_{12}}{\mathbf{J}}\frac{\partial\phi}{\partial\eta}\right)+\frac{\partial}{\partial\eta}\left(\Gamma_\phi\frac{B_{21}}{\mathbf{J}}\frac{\partial\phi}{\partial\xi}\right)+\mathbf{J}S_\phi.\end{aligned} \tag{2}$$

The present equations, in which the Dufour and Soret effects have been neglected, arose through a series of transformations of the derivatives from the Cartesian X_i into the generalized (curvilinear) coordinate system ξ_j, following the procedure described by Ferziger and Perić [27]. [1]

In the above equations the following symbols have been used [27]:

$$B_{mj}=\beta^{1j}\beta^{1m}+\beta^{2j}\beta^{2m},$$

$$U_1=\beta^{11}U+\beta^{21}V,\quad U_2=\beta^{12}U+\beta^{22}V,$$

$$\beta^{11}=\frac{\partial Y}{\partial\eta},\quad \beta^{12}=-\frac{\partial Y}{\partial\xi},\quad \beta^{21}=-\frac{\partial X}{\partial\eta},\quad \beta^{22}=\frac{\partial X}{\partial\xi}.$$

The Cartesian velocity components are computed as

$$U=\frac{\partial\Psi}{\partial Y}=\frac{1}{\mathbf{J}}\left(\beta^{21}\frac{\partial\Psi}{\partial\xi}+\beta^{22}\frac{\partial\Psi}{\partial\eta}\right),$$

$$V=-\frac{\partial\Psi}{\partial X}=-\frac{1}{\mathbf{J}}\left(\beta^{11}\frac{\partial\Psi}{\partial\xi}+\beta^{12}\frac{\partial\Psi}{\partial\eta}\right).$$

The form of the functions P and Q in Eq. (1), which are the so-called control functions can be found in Ref. [15], whereas the diffusion coefficient Γ_ϕ and the source term S_ϕ for each variable of Eq. (2) are defined in Table 1. The source term S_{RS} in the vorticity equation arising from the Reynolds stresses, along with its derivation which is somewhat lengthy, may also be found in Ref. [15] and is not repeated here for the sake of brevity. The source term S_{B} due to buoyancy forces has a new component here owing to concentration gradient effects and is equal to

$$S_{\mathrm{B}}=-Ra\,Pr\left(\frac{1}{\mathbf{J}}\right)\left[\left(\beta^{21}\frac{\partial\theta}{\partial\xi}+\beta^{22}\frac{\partial\theta}{\partial\eta}\right)+N\left(\beta^{21}\frac{\partial C}{\partial\xi}+\beta^{22}\frac{\partial C}{\partial\eta}\right)\right]. \tag{3}$$

As far as the turbulence modeling is concerned, the present approach is essentially of the TRANS (transient Reynolds-averaged-Navier–Stokes) type, similar to the one described by Hanjalić and Kenjereš [28], except that here a two-equation k–ϵ model is used and no second moments are modeled. In unsteady turbulent-flow simulations, and particularly when large-scale or deterministic unsteady phenomena are known to be present such as, for instance, in Rayleigh–Bénard convection [28] or vortex shedding [29], the time-dependent value of the transported quantity $\Phi(t)$ may be thought of as composed of the following three components:

$$\Phi(t)=\underbrace{\bar{\Phi}}_{\text{time-mean component}}+\underbrace{\tilde{\Phi}(t)}_{\text{time-periodic component}}+\underbrace{\Phi'(t)}_{\text{turbulent fluctuation}}. \tag{4}$$

Table 1
Diffusion coefficients Γ_ϕ and source terms S_ϕ for variable ϕ in the generic transport equation, Eq. (2)

ϕ	Γ_ϕ	S_ϕ
Ω	Pr[a]	$S_{\mathrm{B}}+S_{\mathrm{RS}}$
θ	$1+\nu_t^*(Pr/\sigma_{\mathrm{T}})$	0
C	$1/Le+\nu_t^*(Pr/\sigma_{\mathrm{C}})$	0
k	$Pr(1+\nu_t^*/\sigma_k)$	$P_k+G_k-\epsilon$
ϵ	$Pr(1+\nu_t^*/\sigma_\epsilon)$	$C_1f_1P_k(\epsilon/k)+C_3G_k(\epsilon/k)-C_2f_2(\epsilon^2/k)$

The detailed form of quantities S_{RS} and P_k involved in the source terms may be found in Ref. [15].

[a] Note that in this particular case the contribution of ν_t^* is more conveniently included in the source term.

---

[1] Where Y is here the horizontal distance and X the vertical.

The first two components are here incorporated into the symbol ϕ of Eq. (2), while the third one is treated by the Reynolds averaging. The notation $\langle \Phi \rangle(t)$ for the first two components is often used and the arising new component is called a *phase-averaged or ensemble-averaged* [28,29] quantity. However, in the present case, since only a portion of the entire set of turbulent-flow results are unsteady while many of them are steady, the use of a new symbol was not found necessary. It should nevertheless be kept in mind that whenever the numerical solution yields unsteady results, the symbol for each variable ϕ in Eq. (2) or Ψ in Eq. (1) stands for the sum of the first two components of Eq. (4).

The turbulent viscosity is obtained from:

$$\nu_\mathrm{t}^* = \Gamma_\Omega f_\mu C_\mu \frac{k^2}{\epsilon}, \tag{5}$$

The turbulent fluxes for heat and mass transport are computed from the standard gradient diffusion hypothesis (SGDH) as follows:

$$-\overline{u_\mathrm{i}'\theta'} = \frac{\nu_\mathrm{t}^*}{\sigma_\mathrm{T}}\left(\frac{\partial \theta}{\partial X_\mathrm{i}}\right), \quad -\overline{u_\mathrm{i}'C'} = \frac{\nu_\mathrm{t}^*}{\sigma_\mathrm{C}}\left(\frac{\partial C}{\partial X_\mathrm{i}}\right), \tag{6}$$

where here both the turbulent Prandtl number σ_T and the turbulent Schmidt number σ_C are taken as constant and their value is defined below.

Previous experience with turbulence models for natural convection has shown that when using the k–ϵ model in the standard form, overprediction of the heat transfer from the wall is obtained and this could be improved with the use of low-Reynolds terms in the model [30]. Therefore, the present code has mostly focused in incorporating low-Re models for turbulent-flow computations of natural convection, a comparative assessment of which has been presented in a previous study [31]. The model of Launder and Sharma [32] has shown a fairly good accuracy in that assessment, particularly as far as the wall heat transfer is concerned, and was therefore selected for the computations in the earlier study of the solar still problem where only thermal buoyancy effects were considered [15]. It was also used successfully by van der Eyden et al. [21] in a double-diffusive natural convection study and was therefore considered a good choice for the present problem. The damping functions appearing in Eq. (5) and in Table 1 are defined as follows:

$$f_\mu = \exp\left[\frac{-3.4}{(1.0 + Re_\mathrm{t}/50)^2}\right],$$

$$f_1 = 1.0, \quad f_2 = 1.0 - 0.3\exp(-Re_\mathrm{t}^2),$$

whereas the constants of the model are assigned the following values: $C_\mu = 0.09$, $C_1 = 1.44$, $C_2 = 1.92$, $\sigma_k = 1.0$, $\sigma_\epsilon = 1.3$ and $\sigma_\mathrm{T} = \sigma_\mathrm{C} = 0.9$. For C_3 the following expression is used: $C_3 = \tanh|V/U|$ [30] and the turbulence Reynolds number in terms of dimensionless variables is $Re_\mathrm{t} = \Gamma_\Omega(k^2/\epsilon)$. A new term that arises here in the production of turbulent kinetic energy G_k in this double-diffusion case is the contribution of the concentration (solutal) buoyancy forces. This term, in view of Eq. (6), can be written in Cartesian coordinates as:

$$\begin{aligned} G_k &= -Ra\,Pr\frac{\nu_\mathrm{t}^*}{\sigma_\mathrm{T}}\frac{\partial \theta}{\partial Y} - Ra_\mathrm{C}\,Pr\frac{\nu_\mathrm{t}^*}{\sigma_\mathrm{C}}\frac{\partial C}{\partial Y} \\ &= -Ra\,Pr\left[\frac{\nu_\mathrm{t}^*}{\sigma_\mathrm{T}}\frac{\partial \theta}{\partial Y} + N\frac{\nu_\mathrm{t}^*}{\sigma_\mathrm{C}}\frac{\partial C}{\partial Y}\right], \end{aligned} \tag{7}$$

and in the curvilinear coordinate system:

$$\begin{aligned} G_k = -Ra\,Pr\left(\frac{1}{\mathbf{J}}\right)&\left[\frac{\nu_\mathrm{t}^*}{\sigma_\mathrm{T}}\left(\beta^{21}\frac{\partial \theta}{\partial \xi} + \beta^{22}\frac{\partial \theta}{\partial \eta}\right)\right. \\ &\left. + N\frac{\nu_\mathrm{t}^*}{\sigma_\mathrm{C}}\left(\beta^{21}\frac{\partial C}{\partial \xi} + \beta^{22}\frac{\partial C}{\partial \eta}\right)\right]. \end{aligned} \tag{8}$$

2.2. Boundary conditions

Non-slip, impermeable surfaces are taken at all sides, with the vertical ones being adiabatic to both heat and mass transfer, whereas the top and bottom surfaces are isothermal and at constant concentration. Therefore the boundary conditions can be written as

$$\begin{aligned} &U = V = \Psi = 0 \quad \text{at all surfaces,} \\ &\theta = C = 0 \quad \text{and} \quad \theta = C = 1 \quad \text{at the top inclined and} \\ &\quad \text{bottom surfaces respectively,} \\ &\quad \frac{\partial \theta}{\partial X} = \frac{1}{\mathbf{J}}\left(\beta^{11}\frac{\partial \theta}{\partial \xi}\bigg|_w - \beta^{12}\frac{\partial C}{\partial \eta}\bigg|_w\right) = 0 \\ &\quad \text{on the vertical sidewalls,} \\ &\quad \frac{\partial C}{\partial X} = \frac{1}{\mathbf{J}}\left(\beta^{11}\frac{\partial C}{\partial \xi}\bigg|_w - \beta^{12}\frac{\partial C}{\partial \eta}\bigg|_w\right) = 0 \\ &\quad \text{on the vertical sidewalls.} \end{aligned} \tag{9}$$

The wall vorticity is given by the following expression:

$$\begin{aligned} &\Omega_w = \frac{1}{\mathbf{J}}\left(\beta^{11}\frac{\partial V}{\partial \xi}\bigg|_w - \beta^{21}\frac{\partial U}{\partial \xi}\bigg|_w\right) \\ &\quad \text{along the top inclined and bottom surfaces,} \\ &\Omega_w = \frac{1}{\mathbf{J}}\left(\beta^{12}\frac{\partial V}{\partial \eta}\bigg|_w - \beta^{22}\frac{\partial U}{\partial \eta}\bigg|_w\right) \\ &\quad \text{along the vertical side walls.} \end{aligned} \tag{10}$$

For the turbulence variables in the Launder-Sharma model the following values are specified at the wall:

$$k_w = 0, \quad \epsilon_w = 2\Gamma_\Omega\left(\frac{\partial\sqrt{k}}{\partial n}\right)_w^2 = 2\Gamma_\Omega\frac{k_{w+1}}{(\Delta n)^2}, \tag{11}$$

where Δn is the normal wall distance of the first node.

3. Numerical scheme

3.1. General features

The finite-volume-based numerical procedure for solving the equations for the flow field in the $\Psi - \Omega$ formulation along with the energy equation in a curvilinear coordinate system ξ_j has been described by Papanicolaou et al. [15]. The transformed Poisson equation for the stream function, Eq. (1), is solved by the successive over-relaxation (SOR) method, using a nine-point stencil as opposed to the five-point stencil in Cartesian coordinates. The discretized, time-dependent transport equations of the general form expressed by Eq. (2) have to be solved for an additional variable in this case, i.e., the concentration C. The time marching is achieved by means of the alternating-implicit-direction (ADI) method and the arising linear systems of equations are solved using the Thomas or tridiagonal matrix algorithm (TDMA) [27]. The high-order, bounded HLPA scheme [33] was selected for the discretization of the convective terms in the vorticity, energy and concentration equa-

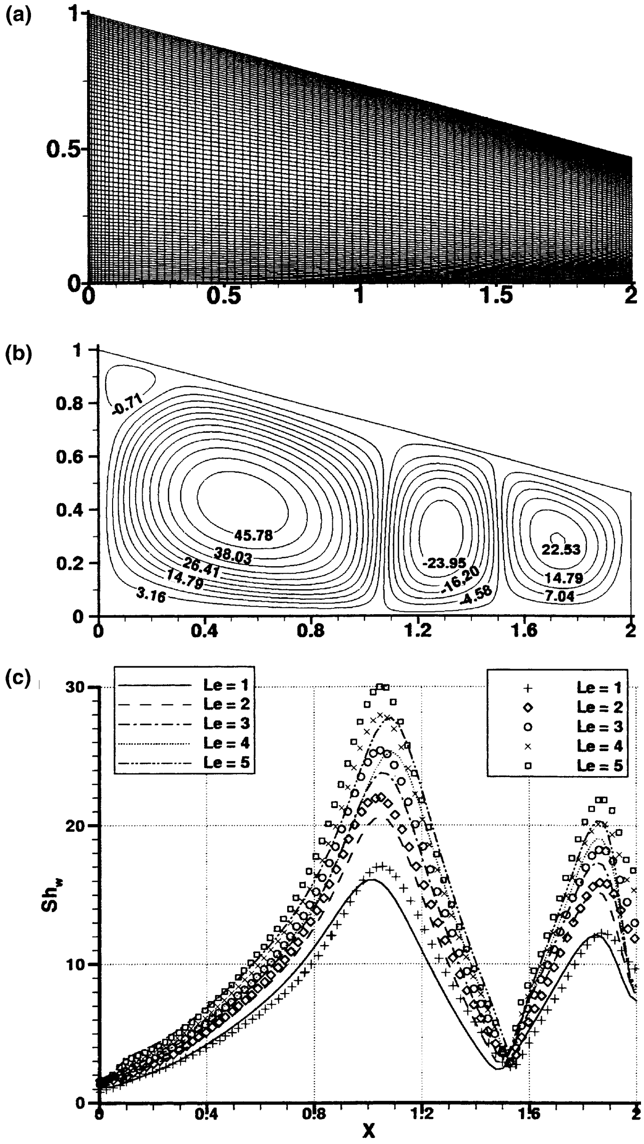

Fig. 2. Trapezoidal enclosure of Boussaid et al. [20] with $L/H = 2$, an inclined top at $\theta = C = 0$ and horizontal bottom at $\theta = C = 1$ used for comparisons. Parameters are: $Gr_H = 8 \times 10^5$ (laminar flow), $N = 1.0$. (a) Present grid, (b) streamlines for $Le = 3$, (c) computed local Sherwood number at the bottom surface (lines) vs. the respective results of Ref. [20] (points).

tions, whereas the power-law scheme [34] was used for the turbulence variables.

3.2. Computational grid-initialization

The curvilinear grid used in the present computations is shown in Fig. 1b. Effort was made to generate a grid which is as orthogonal as possible and with fine resolution near the solid surfaces, so that the thin boundary layers expected are well resolved and the requirements of the low-Re turbulence model are met (wall coordinate $y^+ \leqslant 1$ at the first point from the wall). The grid was successively refined from 61×61 to 91×91 and finally to 121×121, in all cases being non-uniform. The discrepancies between the grid dimensions in terms of selected flow and thermal quantities were compared, considering also the CPU times required on a Pentium III, 600 MHz processor. Between the two finer levels, the discrepancies in turbulent flow ($Ra = 10^9$) were around 1% for the main flow variables and the heat transfer and 2–4% for the turbulence variables, while the CPU times required were shorter by a factor of 2.5–3. Therefore the 91×91 grid was finally selected as a good compromise for all the turbulent-flow computations presented here, whereas in laminar flow computations, the 61×61 non-uniform grid was found adequate in providing grid independence.

Each computation is initialized by using the solution at the immediate lower Rayleigh number as the input. To obtain the solution at the lowest Rayleigh number considered in turbulent flow ($Ra = 10^7$), the velocities, the temperature and concentration are all set to zero initially, while for the turbulence variables a 1% turbulence level was assumed. Using the non-dimensionalized buoyancy velocity ($U_\mathrm{b} = \sqrt{Ra/Pr}$) as a characteristic velocity, the turbulent kinetic energy k is obtained as $k_\mathrm{i} = 0.01^2 \times U_\mathrm{b}^2$. A dissipation length scale is taken from $l_\epsilon = 0.03 \times (L/2)$, yielding a value equal to 0.015 in dimensionless terms. The set of initial values for the turbulence variables is thus completed by taking $\epsilon_\mathrm{i} = k_\mathrm{i}^{3/2}/l_\epsilon$ and computing the turbulent viscosity $\nu^*_{\mathrm{t,i}}$ from Eq. (5). The maximum allowable time step for numerical stability with the chosen grid was equal to 3.0×10^{-8} for most cases, but at higher Rayleigh numbers it had to be reduced to 2.0×10^{-8} or 1.0×10^{-8}. For cases where steady state was eventually attained, approximately 100,000 time steps were required.

3.3. Validation

In the case where thermal buoyancy alone was present [15], the code was validated by comparing against well established numerical solutions for laminar flow in a symmmetric trapezoidal enclosure, differentially heated from the sides. For the present case, similar geometries were sought, preferably with consideration of double-diffusion effects. Unfortunately, relevant experimental and turbulent flow results suitable for comparison purposes are scarce and as the most suitable case the numerical study of Boussaid et al. [20] for laminar flow was selected. Essentially, their geometry may be thought of as resembling the right part of the present geometry, i.e., it has one inclined boundary at the top, at an angle of 15°, horizontal bottom and vertical side walls. Additionally, this case is very relevant in that the driving temperature and concentration gradients are also in the vertical direction with adiabatic vertical side walls. The gradients are such that they give rise to assisting buoyancy forces with $N = 1$. The geometry, along with the corresponding grid used in the present computations and which has the same dimensions as in Ref. [20] (81×81) are shown in Fig. 2a. In Fig. 2b, the computed streamlines using the present code for $Le = 3$ are shown, representative of the flow structure in the enclosure which qualitatively remains almost invariable with Le. In 2c, the bottom surface Sherwood number distribution is compared agadnst the results of Ref. [20] for different Lewis numbers, $Le = 1$–5. Overall, the agreement may be considered satisfactory,

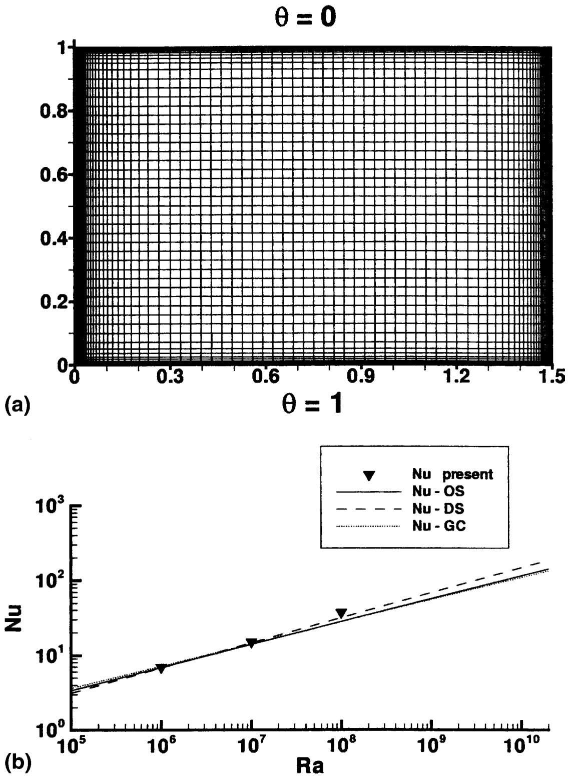

Fig. 3. Rectangular enclosure of Hanjalic et al. [35] with $L/H = 1.5$, bottom heated and with adiabatic side walls used for comparisons in turbulent flow. (a) Present grid, (b) computed mean Nusselt number at the bottom surface (points) for air vs. empirical correlations [36] (lines).

particularly up to $Le = 3$, except in the vicinity of the right vertical wall where the values in Ref. [20] exhibit a relatively strong dependence on Le. Particularly good is the agreement in the location of the overall maxima and minima in the distribution between the two solutions. This indicates a good agreement in the location and size of the flow cells, at the boundaries between which these extreme values occur, a fact which may be inferred by comparing with Fig. 2b. It should be noted that here a boundary-fitted grid is used, while in Ref. [20] the computations were done on a Cartesian grid with a staircase approximation of the inclined boundary.

As far as turbulence modeling, a detailed validation with various models was presented in [31] for a differentially side-heated cavity of aspect ratio $H/L = 5$, using the Cartesian version of the present code. Here additional comparisons are made with the curvilinear version of the code, for a horizontal cavity of aspect ratio $L/H = 1.5$ and with a vertically imposed temperature gradient (heating from below) as more closely related to the problem under investigation. For this case, numerical results were presented by Hanjalic et al. [35] and compared to Nusselt number correlations by different researchers, given by Gebhart et al. [36]. The present re-

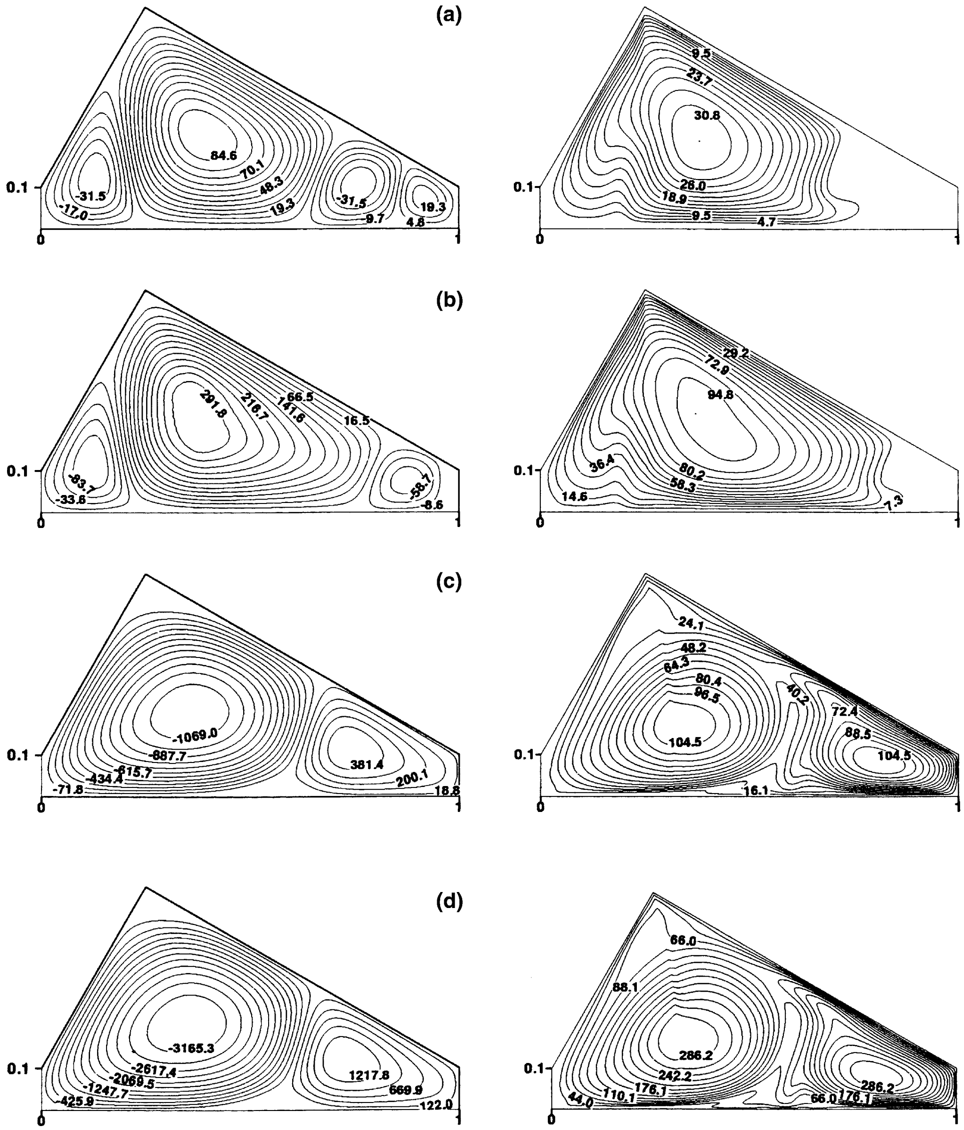

Fig. 4. Computed streamlines (left) and isoviscosity ν_t^* lines (right) at steady state for $N = +1$ in turbulent flow at $Ra = 10^7$ (a), 10^8 (b), 10^9 (c) and 10^{10} (d).

sults are also compared with those correlations, namely the ones by O'Toole and Silveston (OS), Dropkin and Somerscales (DS) and Goldstein and Chu (GC), for air at Rayleigh numbers $Ra = 10^6$–10^8 and using the Launder and Sharma model which was selected for use in this study. In Fig. 3, the computational grid, of dimensions 61 (vertical) × 81 (horizontal) is shown, along with the plot of the computed, steady-state mean Nusselt number at the bottom surface against the Rayleigh number. The agreement is generally good, except at the highest Rayleigh number ($Ra = 10^8$), where the correlations also exhibit discrepancies between one another and the present result appears to follow the DS line closer. In general, the present values (6.89, 14.89 and 36.55 respectively for the three Rayleigh numbers considered) are higher than the values obtained by Hanjalic et al. [35] also with the SGDH approach and closer to the values given by the correlations.

4. Results and discussion

For the mixture air/water vapor, the value of the Schmidt number is $Sc = 0.6$ and thus $Le = 0.86$, whereas the corresponding value $\rho\beta^*$ is equal to +0.61 at 25° and 1 atm [36]. Therefore the sign of N depends on the signs

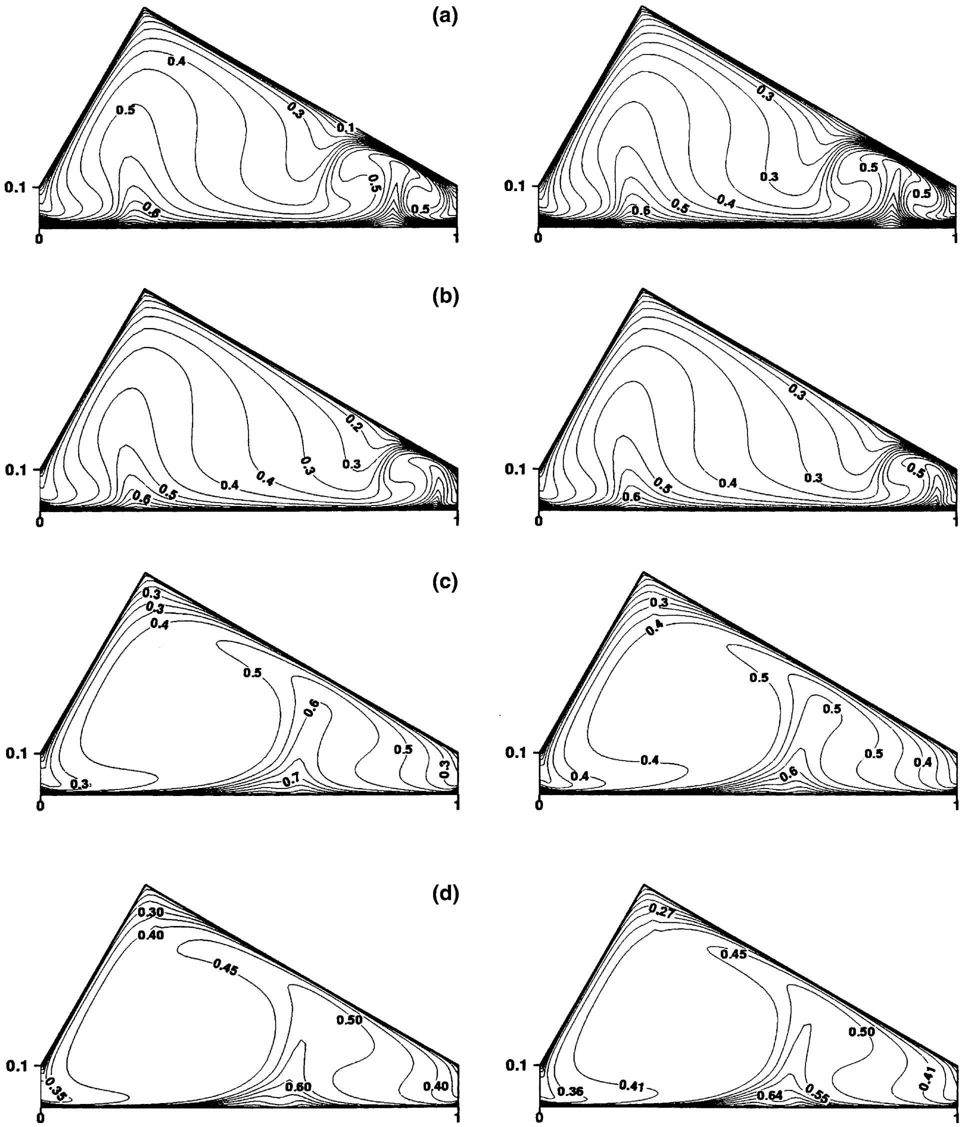

Fig. 5. Computed temperature (left) and concentration (right) contours at steady state for $N = +1$ in turbulent flow at $Ra = 10^7$ (a), 10^8 (b), 10^9 (c) and 10^{10} (d). Twenty levels plotted between 0 and 1.

of ΔT and ΔC. If they are the same, $N > 0$ and if they are opposite, $N < 0$. In order to cover both these possibilities, corresponding to the assisting and opposing buoyancy forces respectively, two simple values were selected, namely $N = 1$ and $N = -1$. Both situations, but the latter case in particular, as has already been mentioned earlier, was known from previous studies to be prone to unsteady, oscillatory behavior, starting at distinct, critical values of *Ra*. Early computations gave indications of a similar behavior also in the present case and it was found necessary to extend the range of investigation to lower values of *Ra* then those in Ref. [15], where a laminar flow simulation was more appropriate. This was dictated by practical considerations as well, since in the specific problem which was the motivation for this study, i.e., the solar still, both positive and negative values of *N* are possible. It is typical of the operation of the still in the morning hours that a temperature-gradient inversion occurs, with the cover attaining a higher temperature than the water in the basin [11]. In this case, there is a negative ΔT and a positive ΔC thus a negative *N*, while the value of ΔT is relatively small due to the low levels of radiation during this period. Therefore, this situation is also characterized by low Rayleigh numbers, where laminar flow is more likely to occur.

4.1. Assisting buoyancy forces

In this case, the two buoyancy forces involved simply add up and this results in a flow field with no major qualitative differences compared to the case with only thermal buoyancy present [15] at the same thermal Rayleigh number. Thus, a flow field characterized by four recirculating cells may be observed at $Ra = 10^7$ in Fig. 4 and by two major cells at $Ra = 10^9$ and $Ra = 10^{10}$. A small deviation occurs at $Ra = 10^8$, where three major cells are present, as opposed to four in Ref. [15], after the major clock-wise rotating cell (positive values of Ψ) has expanded to the right and the rightmost cell has weakened significantly. It is interesting to note that for $Ra \geqslant 10^9$ the counter-clockwise rotating cell dominates, which is a major difference compared to the flow pattern at lower Rayliegh numbers. Quantitatively, there is, as expected, an increase in the magnitude of the flow quantities, such as $\Psi_{\max}$, which increases by approximately 40% compared to the value with thermal buoyancy only present at the respective value of *Ra*. Likewise, the turbulent viscosity, which is plotted in the right column of Fig. 4, increases by 30–40% over the same range of *Ra*. In Fig. 5 the temperature (left) and concentration fields (right) for the same Rayleigh numbers are shown. They look very similar in form at

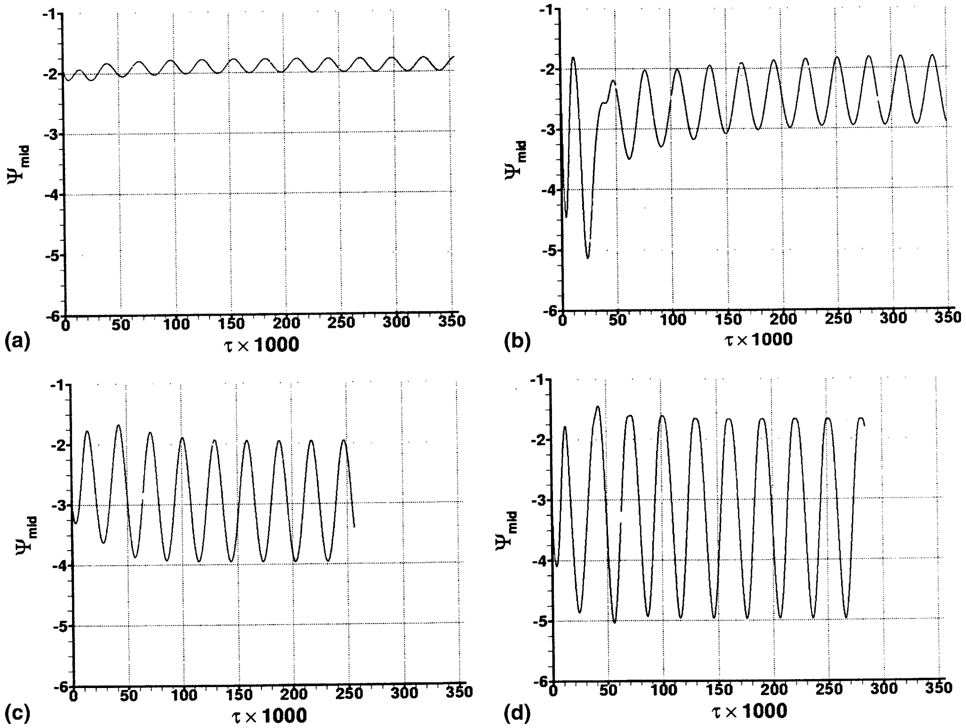

Fig. 6. Periodic behavior of the mid-point stream function with time, for $N = -1$ and laminar flow at $Ra = 4.5 \times 10^6$ (a), 5.0×10^6 (b), 6.0×10^6 (c) and 8.0×10^6 (d).

this value of the Lewis number and, as in Ref. [15], at the smaller values of Ra the distribution looks more uniform, but at higher values large constant-value regions tend to develop at the core, with thinner boundary layers along the solid surfaces.

4.2. Opposing buoyancy forces

In the case of opposing buoyancy forces, the production of turbulence due to buoyancy forces is reduced due to the fact that one of them acts in generating and the other one in destroying turbulence. Therefore, the fact that at both $Ra = 10^7$ and $Ra = 10^8$ early computations using the turbulence model yielded a flow field with zero values of the turbulence variables came to no surprise and could be easily justified. Besides, at these values the solution tends to become unsteady. It appears that the flow at these values is in one of the transition states characterizing the route to turbulence in natural convection problems, particularly those with heating from below, as is very well-known from Rayleigh–Bénard convection. It was therefore decided, before proceeding to the higher end of values of Ra as considered for $N = 1$, to first clarify the observations at the lower end of values, by solving the unsteady laminar-flow equations coupled with the energy and concentration equations. In this effort, it was also found necessary to move backwards by reducing the value of Ra even lower than $Ra = 10^7$, so that a good picture is obtained as to where exactly the steady behavior ceases to exist being succeeded by unsteady phenomena, typical of heating-from-below configurations on one hand, but also of double-diffusive convection problems with opposing buoyancy forces on the other. It is not, however, the intention in this work to fully cover the entire transition-range phenomena, but rather to locate the onset of unsteadiness in laminar flow and then proceed to the fully turbulent regime, as the objective originally was to make comparisons against the cases with $N = 1$ and $N = 0$ [15]. The fully-turbulent regime, characterized by a significant amount of turbulent viscosity, was found to arise only for $Ra \geqslant 10^9$ at $N = -1$ and the relevant results will be presented in a later section.

4.2.1. Laminar flow—oscillatory results

The Rayleigh number was reduced by an order of magnitude, compared to the case with $N = 1$, to $Ra = 10^6$ and the solution that was obtained was found to be steady, a state which was attained at $\tau \approx 0.1$. The flow field is characterized by two strong recirculating cells, with their dividing line intersecting the bottom surface at $Y \approx 0.42$. By gradually increasing Ra to 2×10^6

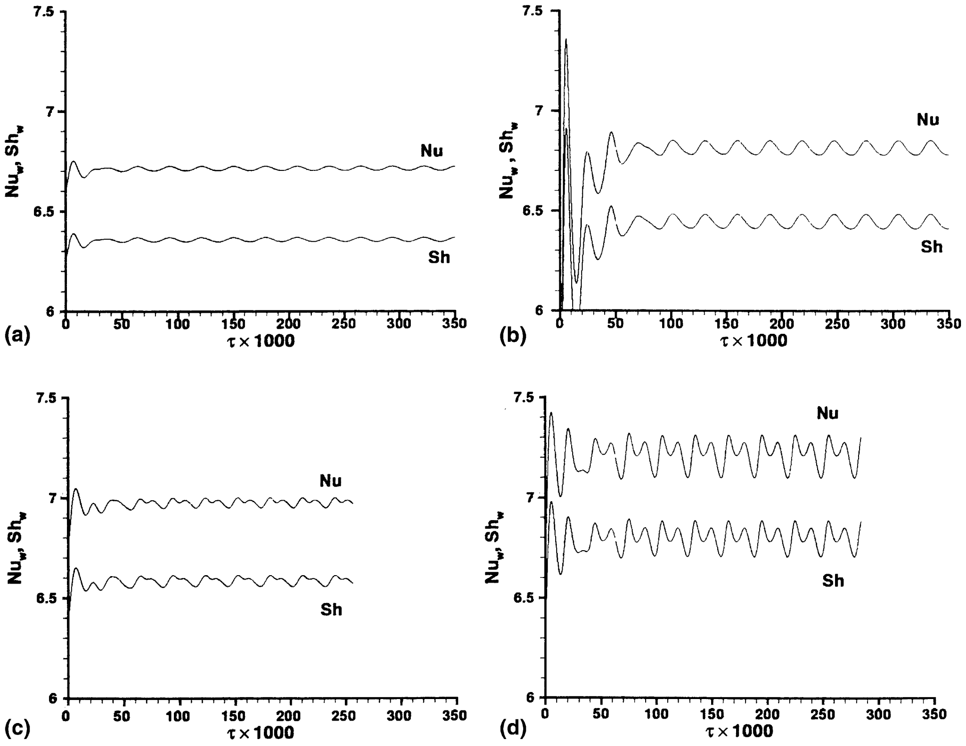

Fig. 7. Periodic behavior of the mean Nusselt and Sherwood number at the bottom surface with time, for $N = -1$ and laminar flow at $Ra = 4.5 \times 10^6$ (a), 5.0×10^6 (b), 6.0×10^6 (c) and 8.0×10^6 (d).

and 3×10^6 steady results are still obtained, with the main cells always being two, and the leftmost one now tilting to the right, even though the bottom surface is still intersected at $Y \approx 0.42$. At $Ra = 4 \times 10^6$, a small cell at the top, just below the edge formed by the two inclined surfaces, makes its appearance in the steady state results which are obtained after a transient period of damped oscillations in the flow quantities. First at $Ra = 4.5 \times 10^6$ these oscillations are found to persist even at large times and no steady state can be obtained. Instead, there is a distinct periodic pattern, observed in several quantities describing the flow field such as, for instance, the midpoint stream function shown in Fig. 6. These oscillations become more intense at the boundary between the leftmost main cell and the new small cell that arises at the top. The oscillations are also present in the mean Nusselt and Sherwood number variation with time in Fig. 7, however the patterns for $Ra \geqslant 6 \times 10^6$ appear somewhat different. Power-spectrum analysis for all variables, using 512 sample points, reveals nevertheless a single dominant frequency and harmonics, a pattern which persists for up to $Ra = 2 \times 10^7$. The power-spectrum analysis for the time histories of $\Psi_{\max}$ of Fig. 6 has the form shown in Fig. 8. In Fig. 9 a typical flow field within one cycle of the oscillations is shown, in terms of stream function contours for $Ra = 8 \times 10^6$ as a representative case. Two major recirculating cells are found to almost maintain their position, but near the top edge a smaller cell alternately makes its appearance and vanishes. This behavior has an effect on the shape and the magnitude of the main cells, even though mostly limited to the top half of the enclosure. It can therefore be concluded that the unsteadiness in the laminar flow regime is due to an instability in the bulk of the flow field, caused by the interaction between the major recirculating cells. The oscillations enter a more irregular state beyond the value of $Ra = 2 \times 10^7$, eventually turning into aperiodic, but the exact evolution from this point to fully-turbulent flow is a subject whose investigation was considered outside the scope of this work.

In order to have an idea of what exactly the effect of the trapezoidal geometry on the oscillatory phenomena is, calculations were performed on an *equivalent* rectangular domain, constructed so as to have an aspect ratio equal to the present one, i.e., $A = H_m/L = 0.3165$, which also yields the same cross-sectional area as the trapezoidal enclosure. Using the same resolution as in the laminar computations for the trapezoidal geometry (i.e., an 61×61 non-uniform grid) and the same physical parameters, the solution that was obtained was of a steady multi-cellular flow for up to $Ra = 6 \times 10^6$. The main flow pattern consisted of a total of six cells, two similar pairs

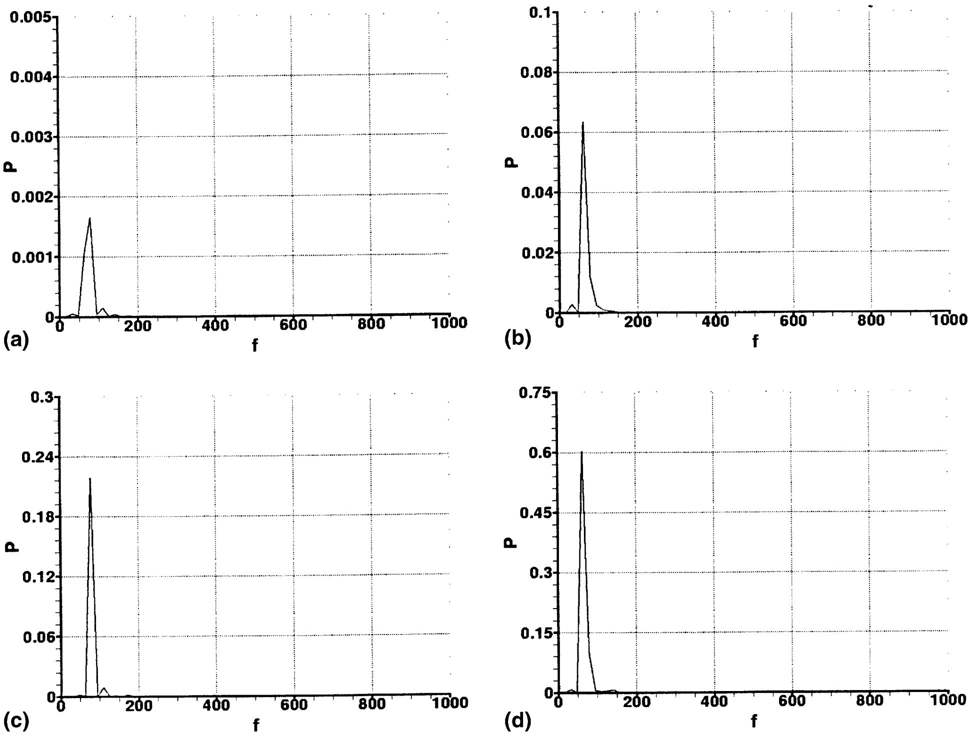

Fig. 8. Power spectrum density vs. frequency for the oscillations of Ψ_{mid} at $N = -1$, and $Ra = 4.5–8 \times 10^6$, for the respective cases shown in Fig. 6.

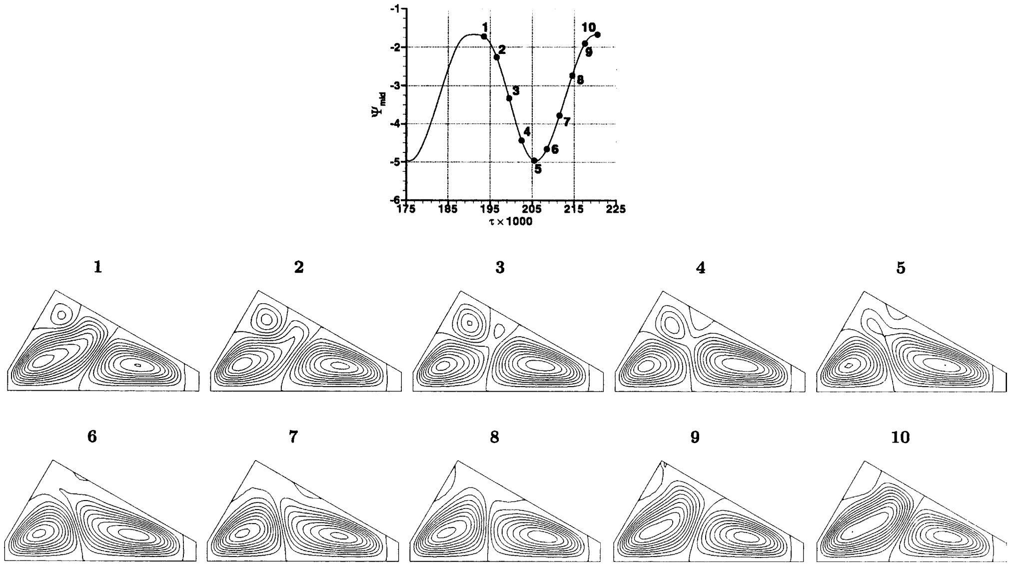

Fig. 9. Computed streamlines at ten different time instants within a period, shown on the Ψ_{mid} vs. dimensionless time curve for $N = -1$, $Ra = 8 \times 10^6$. Contour levels are from −6.4 to 6.4.

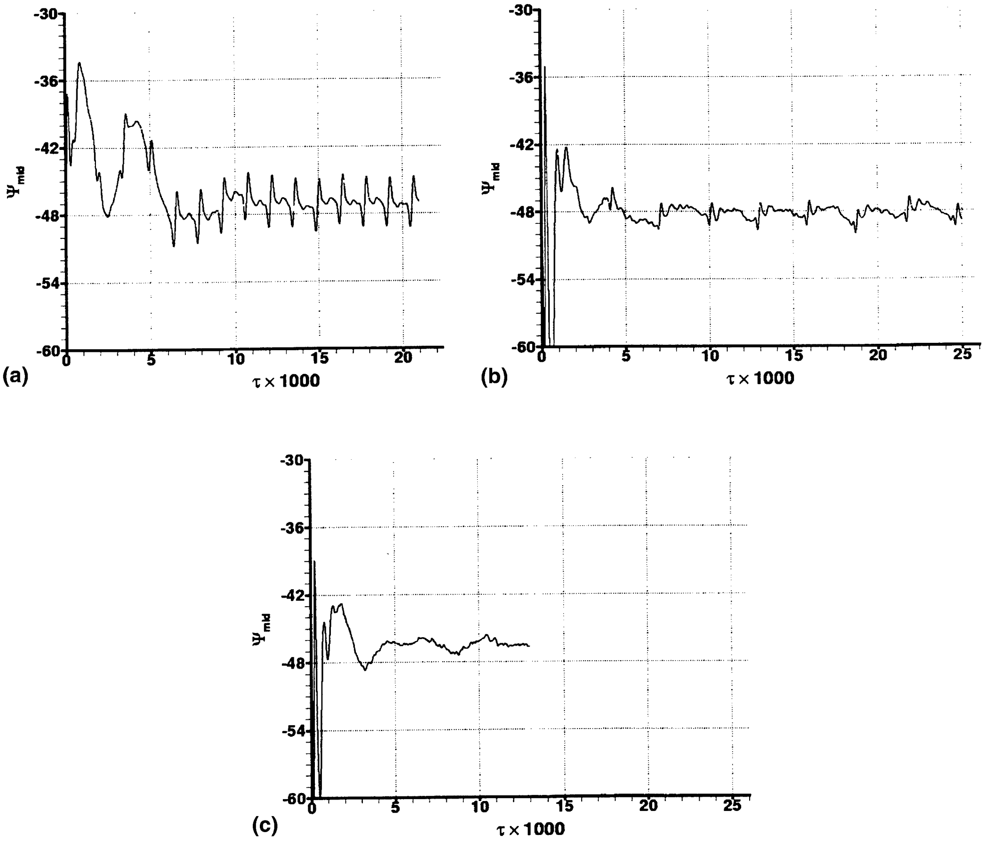

Fig. 10. Variation of the mid-point stream function with time, for $N = -1$ and turbulent flow at: (a) $Ra = 10^{10}$, (b) $Ra = 2.0 \times 10^{10}$ and (c) $Ra = 3.0 \times 10^{10}$.

of counter-rotating inner cells and two end cells of larger size, adjacent to each of the side walls. The wavelength of the inner cells (based on the height of the enclosure) was approximately equal to 0.9, a value which appears very similar to the results obtained by Wee et al. [16], also for opposing buoyancy forces and the same Lewis number, in a horizontal cavity of aspect ratio 1/7 and at $Gr = 5.5 \times 10^5$. In the present case, some small corner vortices did also appear near the top surface and grew in size with increasing Ra, however this increase was not significant so as to disturb the main cells until Ra increased to $Ra = 6.5 \times 10^6$. At this value, and at large times ($\tau \geqslant 0.1$), an oscillatory pattern was obtained, which however did not exhibit any distinct frequency but was rather aperiodic. The number of cells was changing constantly and symmetry was lost. The same behavior was observed for up to $Ra = 8 \times 10^6$ which was the highest value considered. These preliminary findings indicate that the rectangular geometry itself requires a more thorough study which the present limited space does not allow. It can nevertheless be already concluded that the trapezoidal geometry has some own unique features that distinguish it from an equivalent rectangular geometry as far as the onset of unsteadiness is concerned, and tends to transition to a regular periodic regime earlier, boundary conditions and physical parameters being kept otherwise the same between the two geometries.

4.2.2. Turbulent flow results

First at $Ra = 10^9$ a significant amount of turbulent viscosity develops, but the solution does not reach a steady state even at large times, exhibiting irregular oscillations. At $Ra = 5 \times 10^9$ the oscillations become more and more regular, even though still aperiodic, while at $Ra = 10^{10}$ a quasi-periodic pattern establishes,

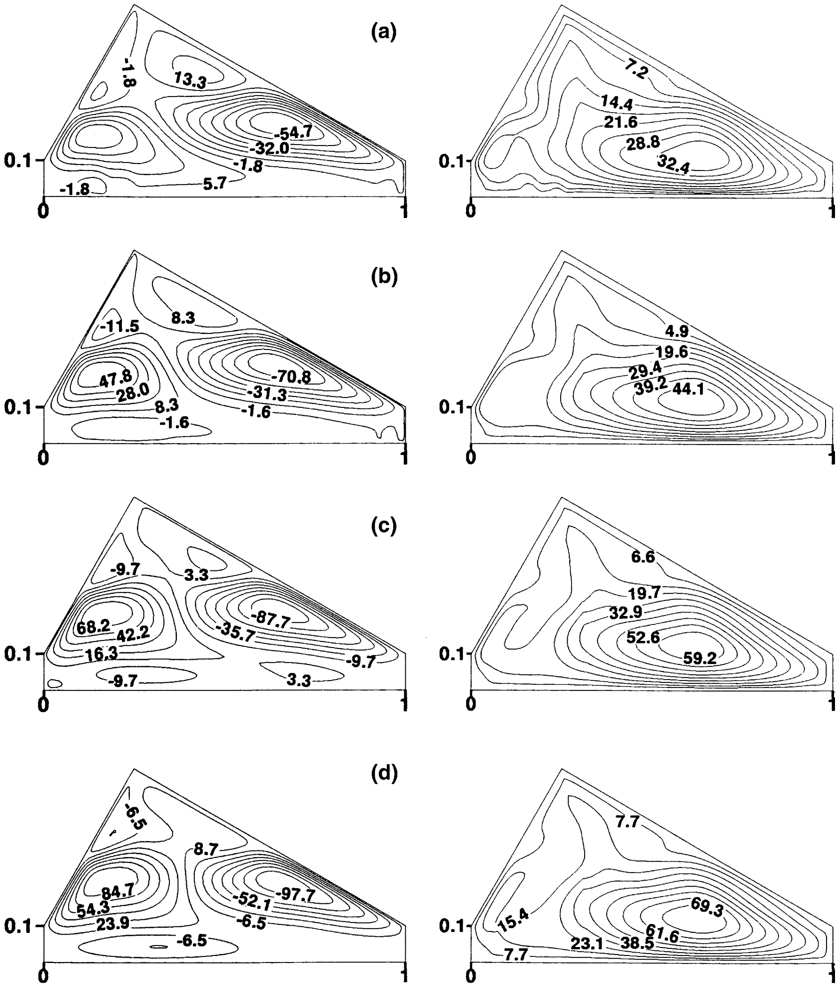

Fig. 11. Computed streamlines (left) and isoviscosity ν_t^* lines (right) at large times for turbulent flow with $N = -1$ and $Ra = 5 \times 10^9$ (a), 10^{10} (b), 2×10^{10} (c) and 3×10^{10} (d).

after an initial transient period. This may be observed in terms of the time histories of the midpoint stream function shown in Fig. 10. With an increase in the value of *Ra*, the oscillations decrease in amplitude, until at $Ra = 3 \times 10^{10}$ an almost steady state is attained within a relatively short period of time. The corresponding plots of the field variables are shown in Figs. 11 and 12, including those for $Ra = 5 \times 10^9$, where instantaneous data are shown. As far as the flow field is concerned (Fig. 11), two major flow cells are still visible, occupying the middle part of the enclosure. However, comparing this to the laminar-flow results, the major cells appear now detached from the bottom surface, where there is significant secondary flow activity. This may be related to the horizontal motion of thermals near horizontal boundaries, a phenomenon described in the study by Chu and Goldstein [37], after their experimental observations of turbulent natural convection in a layer of water. With the increase in the value of *Ra*, the bottom cells become more stable and the solution leads to a steady state at $Ra = 3 \times 10^{10}$. At this value, there is a significant amount of turbulent viscosity, as shown on the right part of Fig. 11, however much less in magnitude than for $N = 1$, as may be observed by comparing the values shown in Fig. 4.

The temperature and concentration fields in Fig. 12 exhibit a similar form, characterized by a stratification pattern and appear less distorted than those of Fig. 5, with no distinct plume-like regions. Some small disturbances may be observed at the left part of the bottom surface for $Ra = 5 \times 10^9$, indicative of the unsteadiness that is still present and which gradually vanishes afterwards. The unsteady behavior and its localized nature may be better realized in Figs. 13 and 14. These are plots of the time histories of the local horizontal velocity component V and the temperature θ, along the same grid line

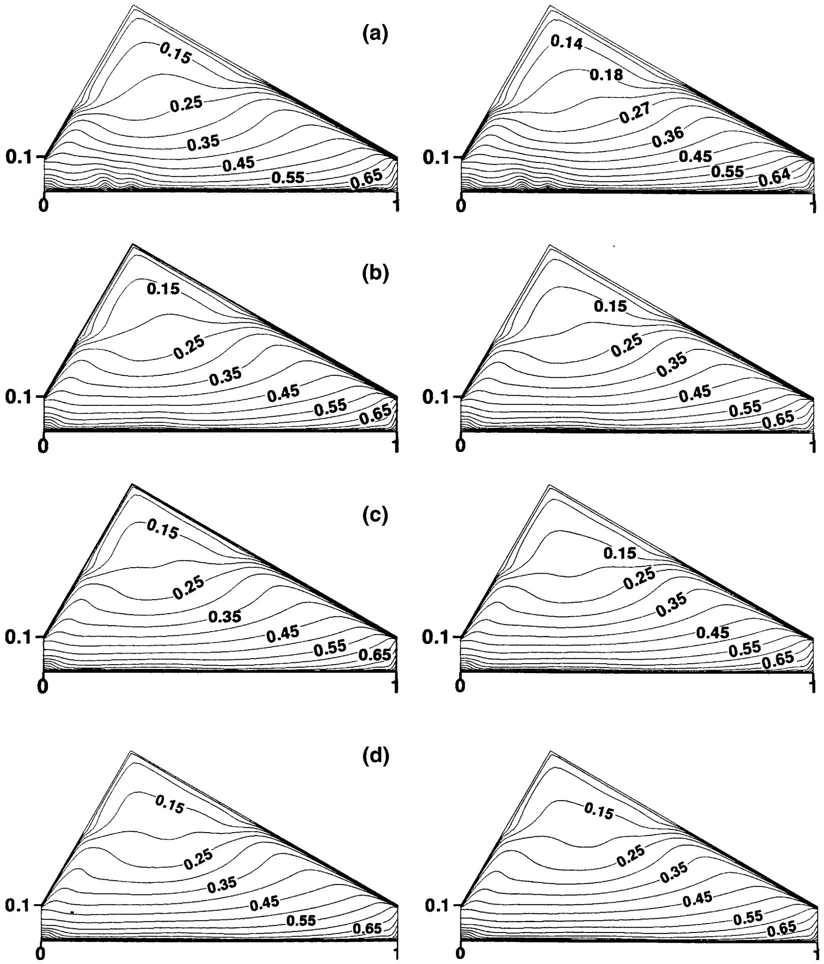

Fig. 12. Computed temperature (left) and concentration (right) contours at large times for $Ra = 5 \times 10^9$ (a), 10^{10} (b) 2×10^{10} (c), and 3×10^{10} (d). Twenty levels plotted between 0 and 1.

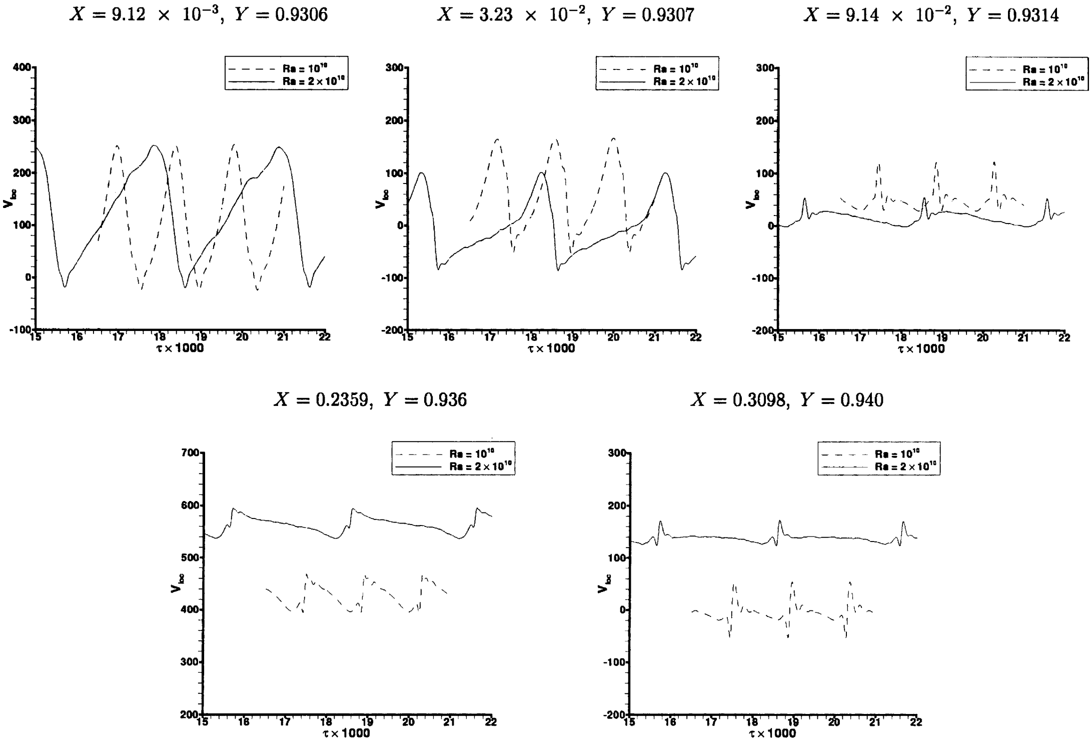
$X = 9.12 \times 10^{-3}$, $Y = 0.9306$ $X = 3.23 \times 10^{-2}$, $Y = 0.9307$ $X = 9.14 \times 10^{-2}$, $Y = 0.9314$

$X = 0.2359$, $Y = 0.936$ $X = 0.3098$, $Y = 0.940$

Fig. 13. Oscillatory behavior of the horizontal velocity component for $N = -1$ and $Ra = 10^{10}$–2×10^{10} at five different locations near the right vertical wall with respective coordinates shown.

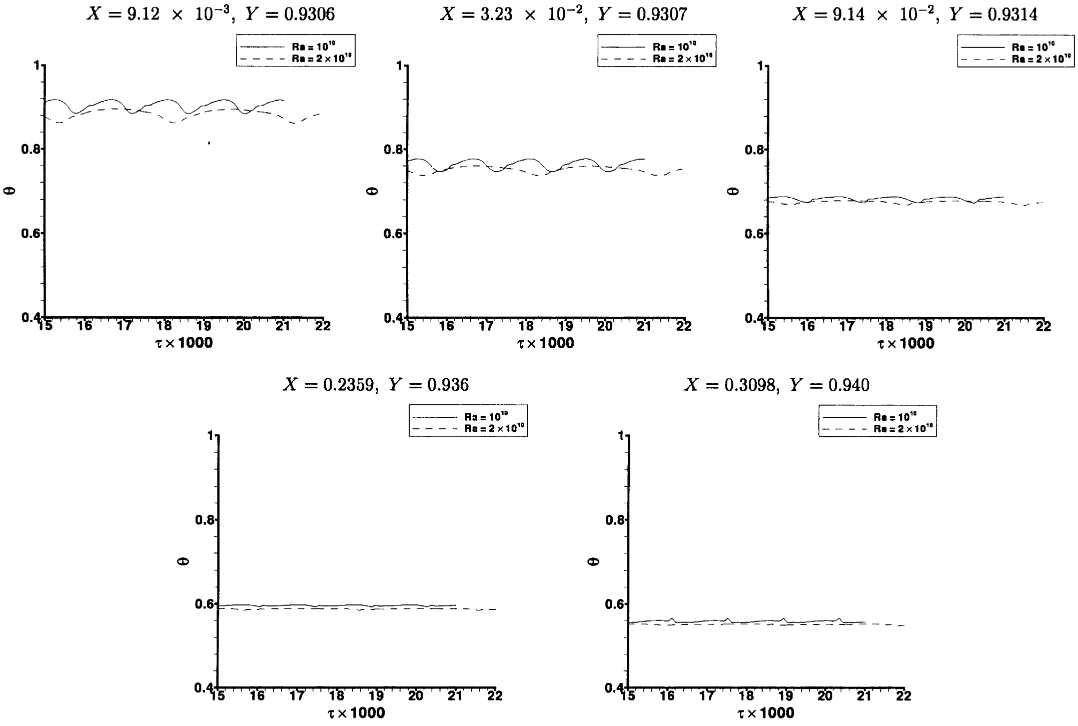
$X = 9.12 \times 10^{-3}$, $Y = 0.9306$ $X = 3.23 \times 10^{-2}$, $Y = 0.9307$ $X = 9.14 \times 10^{-2}$, $Y = 0.9314$

$X = 0.2359$, $Y = 0.936$ $X = 0.3098$, $Y = 0.940$

Fig. 14. Oscillatory behavior of the temperature for $N = -1$ and $Ra = 10^{10}$–2×10^{10} at five different locations near the right vertical wall with respective coordinates shown.

perpendicularly intersecting the bottom surface at $Y \approx 0.93$ (near the right end wall, where the phenomena were found to be more prominent) and extending upwards towards the right inclined surface. Five locations with increasing vertical coordinate (X) are chosen along this line and their coordinates are shown in Figs. 13 and 14. Interesting regular oscillating patterns may be observed for the velocity in Fig. 13, for both $Ra = 10^{10}$ and $Ra = 2 \times 10^{10}$, with amplitudes which vary with height and frequencies which vary with the Rayleigh number. The same may be also said of the temperature in Fig. 14, although overall the amplitudes are smaller. The fact that the amplitudes are larger near the bottom surface constitutes good evidence that the phenomenon relates to the Chu and Goldstein observations [37] of horizontal motion of thermals in that location, further enhanced by the fact that here these thermals appear to originate at fixed locations, exactly as stated in Ref. [37]. However, in the present case the double-diffusive effects play a dominant role, since this unsteady behavior occurs only for $N = -1$. In the turbulent-flow case with opposing buoyancies, therefore, and compared to the laminar flow results presented earlier with its relatively large-scale unsteady phenomena, it can be concluded that the unsteadiness is due to release and horizontal movement of thermals at specific locations along the bottom surface, having thus a more localized character.

4.3. Global flow quantities—heat and mass transfer results

In Fig. 15 some global, characteristic quantities are plotted as a function of the Rayleigh number Ra_m which is based on the mean height of the enclosure. Results for three different values of the buoyancy ratio can be compared, $N = 0$ from Ref. [15], $N = -1$ and $N = 1$ from the present study. The flow quantities Ψ_{max} and $v^*_{t\ max}$ are shown to follow the same rate of increase with Ra_m for $N = 0$ and $N = 1$, even though the magnitude for $N = 1$ is, as expected, higher. The kink in the $v^*_{t\ max}$ curve, due to the flow-pattern transition and the change in the number of flow cells, is also evident in both cases. For $N = -1$ on the other hand, the values and the overall behavior are much different, due to the fact that the two buoyancy forces act against one another and the turbulent regime sets in much later. The same pattern

Table 2
Correlation coefficients for the mean Nusselt and Sherwood numbers in Eqs. (12) and (13)

Coefficient	$N = 0$	$N = 1$	$N = -1$
a	0.418	0.528	0.088
b	0.326	0.326	0.308
c	N/A	0.508	0.099
d	N/A	0.324	0.297

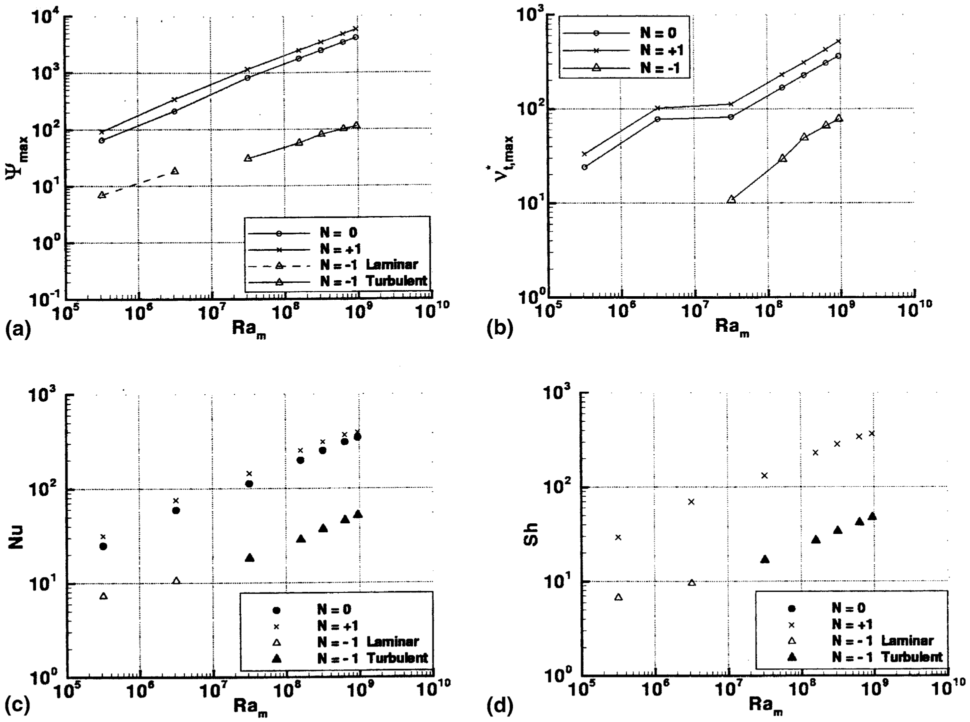

Fig. 15. Variation of selected quantities with Ra_m for various values of N: maximum value of stream function Ψ (a), viscosity ratio v^*_t (b) and mean values along the bottom surface of the Nusselt (c) and the Sherwood number (d).

Table 3
Comparison between cases with $N = 1$ and $N = 0$ in terms of selected quantities in turbulent flow

Quantity	$N = 1$	$N = 0$	% Difference	$N = 1$	$N = 0$	% Difference
Ra	5.000E+09	1.000E+10	–	1.000E+10	2.000E+10	–
Ra_{m}	1.585E+08	3.170E+08	–	3.170E+08	6.341E+08	–
$\overline{Nu}_{\mathrm{b}}$	252.33	252.19	0.06	310.13	311.07	0.30
$\Psi_{\max}$	2483.73	2458.30	1.02	3439.24	3410.70	0.83
Ψ_{mid}	−1955.00	−1944.70	0.53	−2651.90	−2653.20	0.05
$V_{\max}$	29,268.51	28,979.00	0.99	41,067.13	40,710.73	0.87
$U_{\max}$	19,308.24	19,079.43	1.19	27,549.14	27,179.66	1.34
$K_{\max} \times 10^{-6}$	87.806	85.998	2.06	180.200	176.940	1.81
$v^*_{\mathrm{t}\,\max}$	230.16	226.32	1.67	308.23	305.54	0.87
$\epsilon_{\max} \times 10^{-12}$	85.320	83.381	2.27	223.100	217.030	2.72

is observed when comparing the mean values expressing the heat and mass transfer, i.e., the Nusselt and the Sherwood number along the bottom surface. The values computed for $\overline{Nu}$ and $\overline{Sh}$ may be correlated as follows:

$$\overline{Nu} = a \times (Ra_{\mathrm{m}})^b, \tag{12}$$

$$\overline{Sh} = c \times (Ra_{\mathrm{m}})^d, \tag{13}$$

where a, b, c and d factors to be determined. The values that arise in the fully turbulent regime, are shown in Table 2. As may be observed, the exponent in Eq. (12) for $N = 0$ and $N = 1$ is identical and only the multiplying factor a differs. This is consistent with the observation that in the two cases the flow and temperature fields are qualitatively similar (Figs. 4 and 5 and [15]). For $N = -1$ on the other hand, the exponent is somewhat reduced and the coefficient a changes dramatically. The correlation for the Sherwood number has an exponent reduced by roughly 3.8% compared to that for the Nusselt number at $N = 1$ and by 3.6% at $N = -1$, a discrepancy due to the Lewis number effect.

For $N = 1$ in particular, another way of evaluating the Lewis number effect is to compare results for a specific value of the Rayleigh number Ra with double diffusion present against those for thermal buoyancy alone, i.e., $N = 0$, at twice the value of Ra. Such comparisons can be made, for instance, for turbulent flow at $Ra = 5 \times 10^9$ and 10^{10} in the former case, and $Ra = 10^{10}$ and 2×10^{10} respectively in the latter case. The comparisons in terms of selected global quantities are shown in Table 3. The differences that arise for the present value of the Lewis number ($Le = 0.86$) in this range of Ra appear to be small, varying up to a maximum of 1.5% for the main flow quantities and 2.7% for the turbulence quantities, while the effect on the mean Nusselt number at the bottom is less than 0.3%.

5. Conclusions

The double-diffusive natural convection in an asymmetric trapezoidal enclosure with vertical temperature and concentration gradiens has been studied numerically, for both opposing and assisting buoyancy forces ($N = -1$ and $N = 1$). The fluid mixture was humid air and mostly turbulent flow conditions were present. Compared to the results with $N = 0$ of a previous study, the case with $N = 1$ in the range $10^7 \leqslant 10^{10}$ gave a qualitatively almost identical multi-cellular flow structure at the same respective Rayleigh number, albeit with higher heat and mass transfer rates and intensity of recirculation. For $N = -1$, the phenomena are more complex, since the mutually opposing action of the two buoyancy forces leads to a delayed transition to turbulent flow so that at $Ra = 10^7$ the flow is still laminar, but in a periodic oscillatory state, characterized by a single dominant frequency. This unsteadiness sets in at $Ra \approx 4.5 \times 10^6$ and persists for up to $Ra \approx 2 \times 10^7$. Beyond this value the flow becomes gradually aperiodic. In the fully turbulent regime, unsteadiness of a different nature is also observed, with a quasi-periodic behavior but having a more localized effect, particularly evident along the bottom surface. From the above can be inferred that the unsteadiness in the laminar-flow regime is due to interactions between the main flow cells affecting the bulk of the enclosure, whereas in the turbulent flow regime due to thermal release and motion along the bottom surface.

References

[1] F. Moukalled, S. Acharya, Natural convection in trapezoidal cavities with baffles mounted on the upper inclined surfaces, Numer. Heat Transfer, Part A 37 (6) (2000) 545–565.

[2] T. Boulard, C. Kittas, J.C. Roy, S. Wang, Convective and ventilation transfers in greenhouses, part 2: determination of the distributed greenhouse climate, Biosyst. Eng. 83 (2) (2002) 129–147.

[3] P.H. Oosthuizen, Free convective flow in an enclosure with a cooled inclined upper surface, Comput. Mech. 14 (5) (1994) 420–430.

[4] D. Poulikakos, A. Bejan, The fluid dynamics of an attic space, J. Fluid Mech. 131 (1983) 251–269.

[5] S.W. Lam, R. Gani, J.G. Symons, Experimental and numerical studies of natural convection in trapezoidal cavities, ASME J. Heat Transfer 111 (1989) 372–377.

[6] T.S. Lee, Numerical experiments with fluid convection in tilted nonrectangular enclosures, Numer. Heat Transfer, Part A 19 (4) (1991) 487–499.

[7] M. Perić, Natural convection in trapezoidal enclosures, Numer. Heat Transfer, Part A 24 (2) (1993) 213–219.

[8] H. Salmun, Convection patterns in a triangular domain, Int. J. Heat Mass Transfer 38 (2) (1995) 351–362.

[9] R.A. Kuyper, C.J. Hoogendoorn, Laminar natural convection flow in trapezoidal enclosures, Numer. Heat Transfer, Part A 28 (1) (1995) 55–67.

[10] V.B. Shanna, S.C. Mullick, Estimation of heat-transfer coefficients, the upward heat flow and evaporation in a solar still, ASME J. Solar Energy Eng. 113 (1) (1991) 36–41.

[11] K. Voropoulos, E. Mathioulakis, V. Belessiotis, Transport phenomena and dynamic modelling in greenhouse-type solar stills, Desalination 129 (3) (2000) 273–281.

[12] J. Rheinländer, Numerical calculation of heat and mass transfer in solar stills, Solar Energy 28 (2) (1982) 173–179.

[13] A. Palacio, J.L. Fernandez, Numerical analysis of greenhouse-type solar stills with high inclination, Solar Energy 50 (6) (1993) 469–476.

[14] B. Djebedjian, M. Abou Rayan, Theoretical investigation on the performance prediction of solar still, Desalination 128 (2) (2000) 139–145.

[15] E. Papanicolaou, K. Voropoulos, V. Belessiotis, Natural convective heat transfer in an asymmetric, greenhouse-type solar still—effect of angle of inclination, Numer. Heat Transfer, Part A 42 (8) (2002) 855–880.

[16] H.K. Wee, R.B. Keey, M.J. Cunningham, Heat and moisture transfer by natural convection in a rectangular cavity, Int. J. Heat Mass Transfer 32 (9) (1989) 1765–1778.

[17] C. Béghein, F. Haghighat, F. Allard, Numerical study of double-diffusive natural convection in a square cavity, Int. J. Heat Mass Transfer 35 (4) (1992) 833–846.

[18] Z.F. Dong, M.A. Ebadian, Investigation of double-diffusive natural convection in a trapezoidal enclosure, ASME J. Heat Transfer 116 (2) (1994) 492–495.

[19] M. Boussaid, A. Mezenner, M. Bouhadef, Convection naturelle de chaleur et de masse dans une cavité trapézoïdale, Int. J. Thermal Sci. 38 (4) (1999) 363–371.

[20] M. Boussaid, A. Djerrada, M. Bouhadef, Thermosolutal transfer within trapezoidal cavity, Num. Heat Transfer, Part A 43 (4) (2003) 431–448.

[21] J.T. van der Eyden, Th.H. van der Meer, K. Hanjalić, E. Biezen, J. Bruining, Double-diffusive natural convection in trapezoidal enclosures, Int. J. Heat Mass Transfer 41 (13) (1998) 1885–1898.

[22] K. Ghorayeb, A. Mojtabi, Double diffusive convection in a vertical rectangular cavity, Phys. Fluids 9 (8) (1997) 2339–2348.

[23] S. Xin, P. Le Quéré, L.S. Tuckerman, Bifurcation analysis of double-diffusive convection with opposing horizontal thermal and solutal gradients, Phys. Fluids 10 (4) (1998) 850–858.

[24] A. Bergeon, K. Ghorayeb, A. Mojtabi, Double diffusive instability in an inclined cavity, Phys. Fluids 11 (3) (1999) 549–559.

[25] K. Ghorayeb, H. Khallouf, A. Mojtabi, Onset of oscillatory flows in double-diffusive convection, Int. J. Heat Mass Transfer 42 (4) (1999) 629–643.

[26] M. Mamou, P. Vasseur, M. Hasnaoui, On numerical stability analysis of double-diffusive convection in confined enclosures, J. Fluid Mech. 433 (2001) 209–250.

[27] J. Ferziger, M. Perić, Computational Methods for Fluid Dynamics, Springer-Verlag, Berlin Heidelberg, 1996, pp. 205–245.

[28] K. Hanjalić, S. Kenjereš, T-RANS simulation of deterministc eddy structure in flows driven by thermal buoyancy and Lorentz force, Flow, Turbul. Combust. 66 (2001) 427–451.

[29] G. Bosch, W. Rodi, Simulation of vortex shedding past a square cylinder with different turbulence models, Int. J. Numer. Meth. Fluids 28 (1998) 601–616.

[30] R.A.W.M. Henkes, C.J. Hoogendoorn, Comparison exercise for computations of turbulence natural convection in enclosures, Numer. Heat Transfer, Part B 28 (1) (1995) 59–78.

[31] E. Papanicolaou, V. Belessiotis, Transient natural convection in a cylindrical enclosure at high Rayleigh numbers, Int. J. Heat Mass Transfer 45 (7) (2002) 1425–1444.

[32] B.E. Launder, B.I. Sharma, Application of the energy-dissipation model of turbulence to the calculation of flow near a spinning disc, Lett. Heat Mass Transfer 1 (1974) 131–138.

[33] J. Zhu, A low-diffusive and oscillation-free convection scheme, Commun. Appl. Numer. Meth. 7 (3) (1991) 225–232.

[34] S. Patankar, Numerical Heat Transfer and Fluid Flow, Hemisphere, Washington, 1980, pp. 79–111.

[35] K. Hanjalić, S. Kenjereš, F. Durst, Natural convection in partitioned two-dimensional enclosures at higher Rayleigh numbers, Int. J. Heat Mass Transfer 39 (7) (1996) 1407–1427.

[36] B. Gebhardt, Y. Jaluria, R.L. Mahajan, B. Sammakia, Buoyancy-Induced Flows and Transport, Hemisphere, Washington, 1988 (Chapters 6 and 14).

[37] T.Y. Chu, R.J. Goldstein, Turbulent convection in a horizontal layer of water, J. Fluid Mech. 60 (1973) 141–159.